Three Dimensional Non-Hydrostatic Free-Surface Flow Simulation Over Curved and Sharp Crested Weirs

Athanasios J. Klonidis[1], Johannes V. Soulis[2]

[1]Fluid Mechanics/Hydraulics Division, Department of Civil Engineering, Democritus University of Thrace, Xanthi, 67100, HELLAS
[2]Fluid Mechanics/Hydraulics Division, Department of Civil Engineering, Democritus University of Thrace, Xanthi, 67100, HELLAS

Abstract   A non-hydrostatic, moving grid finite-volume implicit numerical scheme is applied to three-dimensional steady free-surface flows over various crested bedform configurations featuring weirs and spillways. The Navier-Stokes equations are modified by exploiting the pseudo-compressibility technique to couple pressures with velocity components. The position of the free-surface is determined by applying a moving boundary condition through the inclusion of the two-dimensional depth-averaged mass continuity equation. To improve the stability and accuracy of the model a new technique is introduced based on the use of two nested iteration steps. All of the mentioned equations are transformed into non-orthogonal body-fitted coordinate system to enable accurate representation of irregular geometries. Calculated water surface elevations and bottom pressures are compared with available measurements of steady flows over curved and sharp crested weirs. The versatility of the model in properly capturing the non-hydrostatic nature of pressure distribution is emphasized.

Keywords   Non-hydrostatic pressure, finite-volume scheme, implicit numerical scheme, non-orthogonal boundary fitted coordinates, moving grid, steady flow, various crested weirs.

1. Introduction

Numerical modelling of irregular bedforms hydrodynamics is a challenging task. Since hydraulic models are used extensively to visualize and understand the complexity of hydraulic phenomena, their application to water flow simulation over relevant hydraulic structures, like weirs and spillways, contribute significantly to the improvement of such structures design. Generally, on the crest the flow is critical changing quickly to supercritical downstream the crest. In addition, if the crest is followed by a steep, curved bottom, the rapidly developed non-uniform flow forms large streamline curvatures thus resulting into a non-hydrostatic pressure distribution over the bottom surface. From this aspect the use of a 3D model to simulate such flows seems to be a fundamental prerequisite. The evolution of computer technology in the last decade boosted the implementation of 3D models. Various 3D codes were applied to non-hydrostatic flows. Most of them are implemented on fixed grids employing the pressure-velocity decoupling or pressure-linked technique.

Bhajantri and Eldho [1] developed a quasi-3D model based on the weakly compressible equations. The model was used to investigate the hydraulic characteristics of flow over spillway crest profile by simulating the velocity distribution, pressure distribution and discharge characteristics. The developed numerical model was applied to two different types of spillways. Ferrari [2] solved the 3D full weakly compressible Navier–Stokes equations with the equation of state for water. The numerical method used consisted of a new meshless Smooth Particle Hydrodynamics (SPH) formulation that accurately tracks the free-surface profile and provides monotone pressure fields. The model was used to simulate free-surface flow over a sharp-crested weir. Two CFD codes, Flow-3D and SSIIM 2, have been used by Haun et al. [3] to calculate the water flow over a trapezoidal broad-crested weir. Both programs apply different algorithms for making the grid and computing the free water surface. Flow-3D uses the Volume of Fluid (VOF) method with a fixed grid, while SSIIM 2 uses an algorithm based on the continuity equation and the Marker-and-Cell method, together with an adaptive grid for the water surface. The results were compared with measurements from a physical model study, using different discharges.

The present research work constitutes a part of continuously developing algorithm at Democritus University of Thrace, Greece. The model incorporates an implicit scheme which was developed and properly adapted to track the free-surface. The Navier-Stokes equations are coupled with the depth-averaged continuity equation. As a result, the free-surface is treated as a vertically moving boundary. No pressure-velocity decoupling or pressure-linked or any other additional method is needed as the pressure value is calculated directly from the continuity equation, Chorin [4]. All equations are transformed in a non-orthogonal body-fitted coordinate system. During the grid construction, the model determines a fixed number of nodes along the vertical direction which are located equidistantly. As the iterations proceed, the grid moves vertically following the new free-surface position and the grid nodes are rearranged. To overcome the presence of dispersion errors due to rapid grid rearrangement, the model adopts an innovative procedure through which two nested iteration steps are used. All calculations take place within the inner iteration step but, as long as the iterations last, all values referring to the previous iteration remain unchanged. Upon convergence, the outer iteration step takes over to update the flow field. Following this procedure the model becomes highly stable and accurate. The model was used to analyse steady flows over curved and sharp crested weirs. Predicted water surface elevations and bottom pressures are compared with measurements. Emphasis is given to the ability of the model to capture non-hydrostatic pressure distribution.

2. Mathematical and Numerical Formulation

2.1. Governing Flow Equations

The flow is assumed to be homogenous, incompressible, 3D and viscous, with negligible Coriolis and wind forces. The governing Navier-Stokes equations are modified by introducing a factor β in the space derivatives of mass continuity equation while the density in the time derivative is substituted by the pressure. This procedure refers to as the pseudo-compressibility technique, initially introduced by Chorin [4]. After applying this technique, the system of Navier-Stokes equations becomes:

$$
\frac{\partial P}{\partial t} + \frac{\partial(\beta\rho v_i)}{\partial x_i} = 0
$$
$$
\frac{\partial(\rho v_i)}{\partial t} + \frac{\partial(\rho v_j v_i)}{\partial x_j} = -\frac{\partial P}{\partial x_j} + (f_i)_\tau + (f_i)_g
$$
$$(1)$$

where P is the pressure, β is the pseudo-compressibility factor, ρ is the water density while the contravariant indexes i, j of the velocity vector v vary along all three-dimensions. In addition, $(f_i)_\tau$ represents the viscous stresses and $(f_i)_g = -\rho g \partial h / \partial x_i$ stands for the gravitational forces. The turbulent kinematic viscosity appearing in the term $(f_i)_\tau$ is determined with respect to the friction velocity $u*$ on the channel bottom as:

$$
v_\tau = \bar{v}_\tau = 0.1 h u_*
$$
$$
u_* = \frac{\sqrt{\tau_{bx}^2 + \tau_{by}^2}}{\rho}
$$
$$
\tau_{bx} = ghS_{fx}, \quad \tau_{by} = ghS_{fy}
$$
$$(2)$$

h is the vertical distance between free-surface and channel bottom and S_{fx} and S_{fy} are the bottom friction slopes along the x- and y directions, respectively. Their values are determined with respect to the Manning's roughness coefficient. The use of equations (2) is consistent with the types of flow developing in channels with smooth bed and walls as considered in the present work. According to Liu [5], in such flow types apart from the viscous sublayer where the flow is laminar, measurements showed that also in the turbulent logarithmic layer the turbulent shear stress is constant and equal to the bottom

shear stress. Furthermore, by the modification of Prandtl's mixing length assumption, the logarithmic velocity profile applies also both to the transitional layer and the turbulent outer layer. Measured and computed velocities showed reasonable agreement. Therefore, from engineering point of view, even at high Reynolds numbers, a turbulent layer with the logarithmic velocity profile can be adequately assumed that covers the transitional layer, the turbulent logarithmic layer and the turbulent outer layer. With respect to the above, the model adopts a linear distribution of the bottom shear stress, τ_b, over the flow depth taking its higher value at the channel bottom and a zero value on the free-surface.

For the solution of equations (1), regarding the free-surface flow problems, the following boundary conditions are applied:

- The pressure on the free-surface is zero.

- The fluid velocities v_x, v_y, v_z normal to bottom and solid boundaries are set equal to zero.

- During the fluid motion the fluid particles on the free-surface remain on it. Therefore, in the present study, the free-surface is treated as a moving boundary. Its vertical position h, calculated from the channel bottom, is determined by introducing an additional partial differential equation; the depth-averaged continuity equation, Klonidis [6]:

$$\frac{\partial h}{\partial t} + \frac{\partial (h\bar{v}_x)}{\partial x} + \frac{\partial (h\bar{v}_y)}{\partial y} = 0 \tag{3}$$

The main advantage of equation (3) is that it includes the proper boundary conditions at the bottom and at the free-surface. This approach brings a simple and robust method of finding the free-surface location while automatically satisfying the mass conservation criterion.

2.2. Transformation Procedure

According to the proposed finite-volume scheme, hexahedra resulting from the grid construction of the physical domain are transformed to cubes in the computational domain, figure 1. This is accomplished through independent transformations from Cartesian x, y, z or global coordinates to local coordinate system ξ, η, ζ. Each cube in the computational domain comprises eight primary (hexahedra) elements of the physical domain. The secondary element centre is the point where the local coordinate system is initiated ($\xi=0$, $\eta=0$, $\zeta=0$) with ξ, η and ζ ranging between $-1 \leq \xi \leq 1$, $-1 \leq \eta \leq 1$ και $-1 \leq \zeta \leq 1$. Detailed description of the transformation can be found in Klonidis [6].
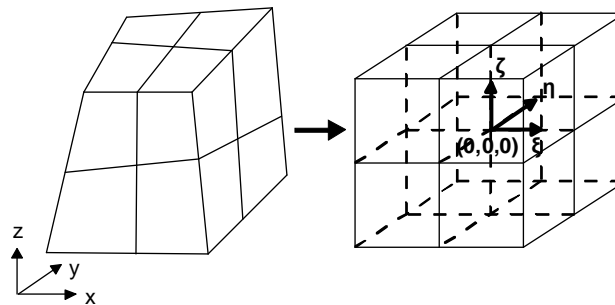

Figure 1. Hexahedra are transformed to cubes. Eight primary elements (hexahedra) shown on the left constitute a secondary element (right).

Under the aforementioned transformation, equation (1) takes the form:

$$\frac{\partial \hat{Q}}{\partial t} + \frac{\partial \hat{F}}{\partial \xi} + \frac{\partial \hat{G}}{\partial \eta} + \frac{\partial \hat{H}}{\partial \zeta} = \frac{\partial \hat{F}_v}{\partial \xi} + \frac{\partial \hat{G}_v}{\partial \eta} + \frac{\partial \hat{H}_v}{\partial \zeta} + \hat{W} \tag{4}$$

$$\hat{Q} = \begin{bmatrix} JP \\ J\rho v_x \\ J\rho v_y \\ J\rho v_z \end{bmatrix}, \quad \hat{F} = \begin{bmatrix} J\beta\rho v_\xi \\ J(\rho v_x v_\xi + P\xi_x) \\ J(\rho v_y v_\xi + P\xi_y) \\ J(\rho v_z v_\xi + P\xi_z) \end{bmatrix}, \quad \hat{G} = \begin{bmatrix} J\beta\rho v_\eta \\ J(\rho v_x v_\eta + P\eta_x) \\ J(\rho v_y v_\eta + P\eta_y) \\ J(\rho v_z v_\eta + P\eta_z) \end{bmatrix}, \quad \hat{H} = \begin{bmatrix} J\beta\rho v_\zeta \\ J(\rho v_x v_\zeta + P\zeta_x) \\ J(\rho v_y v_\zeta + P\zeta_y) \\ J(\rho v_z v_\zeta + P\zeta_z) \end{bmatrix} \quad (5)$$

$$\hat{F}_v = \begin{bmatrix} 0 \\ J\bar{f}_{v2} \\ J\bar{f}_{v3} \\ J\bar{f}_{v4} \end{bmatrix}, \quad \hat{G}_v = \begin{bmatrix} 0 \\ J\bar{g}_{v2} \\ J\bar{g}_{v3} \\ J\bar{g}_{v4} \end{bmatrix}, \quad \hat{H}_v = \begin{bmatrix} 0 \\ J\bar{h}_{v2} \\ J\bar{h}_{v2} \\ J\bar{h}_{v2} \end{bmatrix}, \quad \hat{W} = \begin{bmatrix} 0 \\ 0 \\ 0 \\ J\rho g \end{bmatrix} \quad (6)$$

J is the determinant of the transformation matrix. Other terms have the usual meaning. Detailed description of the viscous terms $\bar{f}_{v2}$, $\bar{g}_{v2}$, $\bar{h}_{v2}$ can be found in Klonidis [6].

In addition to the hydrodynamic equations, the depth-averaged continuity (global 2D), equation (3), also needs to be transformed in the local coordinate system. To solve this equation in the local coordinate system a new 2D computational grid is created. Thus, quadrilaterals in the physical domain are transformed to squares in the computational domain, Klonidis and Soulis [7]. Each square in the computational domain comprises four primary (quadrilaterals) elements of the physical domain. Following the aforementioned procedure the transformed depth-averaged continuity equation takes the form:

$$\frac{\partial(Jh)}{\partial t} + \frac{\partial(Jh\bar{v}_\xi)}{\partial \xi} + \frac{\partial(Jh\bar{v}_\eta)}{\partial \eta} = 0 \quad (7)$$

2.3. Numerical Solution

For the numerical approach of equations (4) a second-order accurate, implicit, finite-difference scheme was developed. The whole process involved the linearization of equations (4) by expanding to Taylor series the time derivatives initially and next the space derivatives. Forward differences were used for time derivatives and central differences for space derivatives. The above procedure yields:

$$\left(I + \frac{\Delta t}{2}\frac{\delta \hat{A}^n}{\Delta \xi}\right)\left(I + \frac{\Delta t}{2}\frac{\delta \hat{B}^n}{\Delta \eta}\right)\left(I + \frac{\Delta t}{2}\frac{\delta \hat{C}^n}{\Delta \zeta}\right)\Delta \hat{Q}^{n+1} =$$
$$-\frac{\Delta t}{2}\left(\frac{\delta \hat{F}^n}{\Delta \xi} + \frac{\delta \hat{G}^n}{\Delta \eta} + \frac{\delta \hat{H}^n}{\Delta \zeta} - \frac{\delta \hat{F}_v^n}{\Delta \xi} - \frac{\delta \hat{G}_v^n}{\Delta \eta} - \frac{\delta \hat{H}_v^n}{\Delta \zeta} - \hat{W}_{i,j}^n\right) \quad (8)$$

δ denotes central difference, I is the identity matrix 4x4 and $\hat{A} = \partial\hat{F}/\partial\hat{Q}$, $\hat{B} = \partial\hat{G}/\partial\hat{Q}$ and $\hat{C} = \partial\hat{H}/\partial\hat{Q}$ are the Jacobian matrices resulting from the linearization procedure. In general, equation (8) is implemented in the following sequence:

$$\left(I + \frac{\Delta t}{2}\frac{\delta \hat{A}^n}{\Delta \xi}\right)\Delta \hat{Q}^{**} = -\frac{\Delta t}{2}\left(\frac{\delta \hat{F}^n}{\Delta \xi} + \frac{\delta \hat{G}^n}{\Delta \eta} + \frac{\delta \hat{H}^n}{\Delta \zeta} - \frac{\delta \hat{F}_v^n}{\Delta \xi} - \frac{\delta \hat{G}_v^n}{\Delta \eta} - \frac{\delta \hat{H}_v^n}{\Delta \zeta} - \hat{W}_{i,j}^n\right) \qquad 1^{st}\ step \quad (9)$$

$$\left(I + \frac{\Delta t}{2} \frac{\delta \hat{B}^n}{\Delta \eta} \right) \Delta \hat{Q}^* = \Delta \hat{Q}^{**} \qquad \qquad 2^{nd} \text{ step} \qquad (10)$$

$$\left(I + \frac{\Delta t}{2} \frac{\delta \hat{C}^n}{\Delta \zeta} \right) \Delta \hat{Q}^{n+1} = \Delta \hat{Q}^* \qquad \qquad 3^{rd} \text{ step} \qquad (11)$$

$$\hat{Q}^{n+1} = \hat{Q}^n + \Delta \hat{Q}^{n+1} \qquad \qquad 4^{th} \text{ step} \qquad (12)$$

The values of the unknown variables at every point of the field are obtained by solving a block tri-diagonal system. The scheme is second-order accurate in space since central differences are used for the space derivatives.

To determine the position of free-surface, the depth-averaged continuity equation is coupled with the hydrodynamic equations and it is approximated by applying the same implicit scheme in 2D form, Klonidis and Soulis [7]. Since the new free-surface level position has been determined, the grid points, which are always located equidistantly along the vertical direction, are rearranged. The resulting curvilinear grid is transformed again into the local system before proceeding in the next iteration step. Extensive numerical experiments confirmed the presence of significant dispersion errors due to grid rearrangement. To overcome this problem a new effective technique was applied; instead of using a single iteration step, two nested ones are used. Let's denote with *"n"* the basic or outer iteration step and with *"k"* the inner one. When the outer iteration starts all Q (P,u,v,w,h) values are initialized. The whole computational procedure, described by equations (9)-(12), takes place within the inner iteration step but as long as the *"k"* iterations last every Q value is calculated as,

$$Q^{k+1} = Q^n + \Delta \hat{Q}^{k+1} \ , \ Q^{k+2} = Q^n + \Delta \hat{Q}^{k+2} \ , ... , \ Q^{k+i} = Q^n + \Delta \hat{Q}^{k+i} \qquad (13)$$

the superscript *k+i* stands for the kth iteration step. The value Q^n, which is referred to the outer iteration, is kept constant during the inner iterations. It should be noted that the grid is rearranged within the inner iterations. The inner iterations continue until the convergence criterion related to the average percentage velocity is satisfied. Next, the outer iteration step changes to the next one and the Q values are updated as follows,

$$Q^{n+1} = Q^{k+i} \ , \ Q^{n+2} = Q^{k+i} \ , ... , \ Q^{n+j} = Q^{k+i} \qquad (14)$$

the superscript *n+j* stands for the nth iteration step. The outer iterations and consequently the whole computational procedure stops when two convergence criteria associated with the average percentage flow depth and the average percentage pressure are satisfied. Generally, the model starts with less than 15 inner iterations, which are decreased rapidly. As much as the outer convergence criterion is satisfied one or maximum two inner iterations are executed.

3. Model Applications

3.1. Free-Surface Flow over a Double Arc Weir

Klonidis and Soulis [6] carried out a series of experiments to study the impacts of steady free-surface flow over a double arc weir model. Both experimental data and predictions are presented in the present report. Measurements were carried out in a 10.0 m long and 0.25 m wide flume with iron bed and plexiglass side walls at Democritus University of Thrace, Greece. A weir model with plexiglass bed consisting of two arcs of R_1=0.71 m and R_2=1.36 m radius, respectively, was mounted in the middle of the flume, as it is shown in figure 2. The crest is defined by two arcs with axial (longitudinal) distances of 0.56 m and 0.78 m, respectively. Thus the total length of the model was 1.34 m. The crest elevation was measured as 0.2691 m. The flume was long enough so that the flow approaching the spillway was fully developed. Holes were drilled on the bottom of

the downstream arc, R_2=1.36 m, with iso-distanses of 0.05 m along the longitudinal direction and 0.03 m along the transverse direction. Thin tubes of an internal diameter 2.0 mm were mounted to measure the bottom static pressure. Appropriately calibrated pressure transducers were utilized. A perpendicular to the bottom surface solid upper wall, made of plexiglass, was placed at distance of 0.125 m from the lower wall on the downstream arc so as its leading edge coincided with the mid-point of the crest width. The upper wall was flared, in relation to the flume axial direction, so as its trailing edge touched the flume's full width, figure. 2. Therefore, an expansion along the downstream arc was created. Also, the upper wall was straightforwardly extended upstream and eventually it was properly curved to meet the full width of the flume. Thus, a relatively smooth water entrance was achieved.
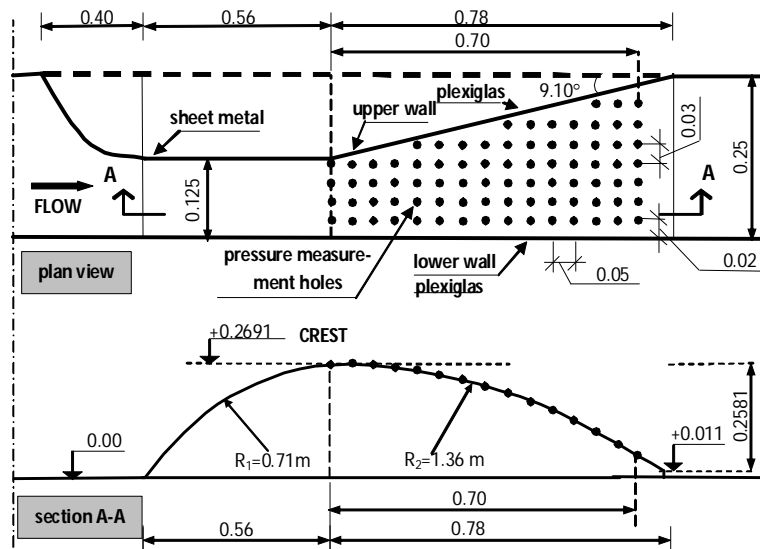

Figure 2. Double arc spillway geometry with static pressure measurements setup. All dimensions in meters.

A series of flow discharges were applied. Current results refer to steady flow discharge, Q=0.0163 m^3 s^{-1}. The water surface elevations above the crest as well as at the outlet of the downstream arc were measured from leveled bottom as 0.391 m and 0.047 m, respectively. Water surface elevations and bottom pressures were measured at each available tapping. The downstream arc of the spillway was simulated by applying the implicit finite-volume scheme. A fine structured grid consisting of hexahedra with a total of 167000 nodes was created. On the crest, a vertical depth equal to 0.129 m (=0.391-0.2691 m) was applied. A constant axial velocity component on the crest was calculated, having the transverse and vertical velocity components equal to zero. Finally, a constant hydrostatic pressure value (= $\rho g h_{in}$) on the crest was calculated, where h_{in}, stands for the water depth on the crest. The flow was critical on the crest turning rapidly to supercritical one at immediately downstream regions. Therefore, the applied boundary conditions corresponded to supercritical flow. A value of 1.0 was given to the pseudo-compressibility factor β determined after numerical experimentation. The Manning's roughness coefficient n was set 0.01 s m$^{-1/3}$ which is consistent with glass made walls and bed. The model captured the water surface elevation along the a) lower wall, b) mid-stream line and c) upper wall. Comparisons with measured data are very satisfactory as shown in figures 3a-3c.

In figures 4a-4c calculated bottom static pressures are compared with the measured data along the, a) lower wall, b) mid-stream line and c) upper wall, respectively. Computed results satisfactorily agree with measurements. Results from the above figures reveal a gradual pressure drop within the first 0.5 m measured downstream to crest. From this position towards to the end of the arc, the pressure drop decelerates. It is also evident that both measured and predicted bottom static pressures significantly diverge from the hydrostatic ones. Finally, it becomes apparent that away from the crest the flow is accelerated. Henceforth, the differences between computed and hydrostatic pressures increase.
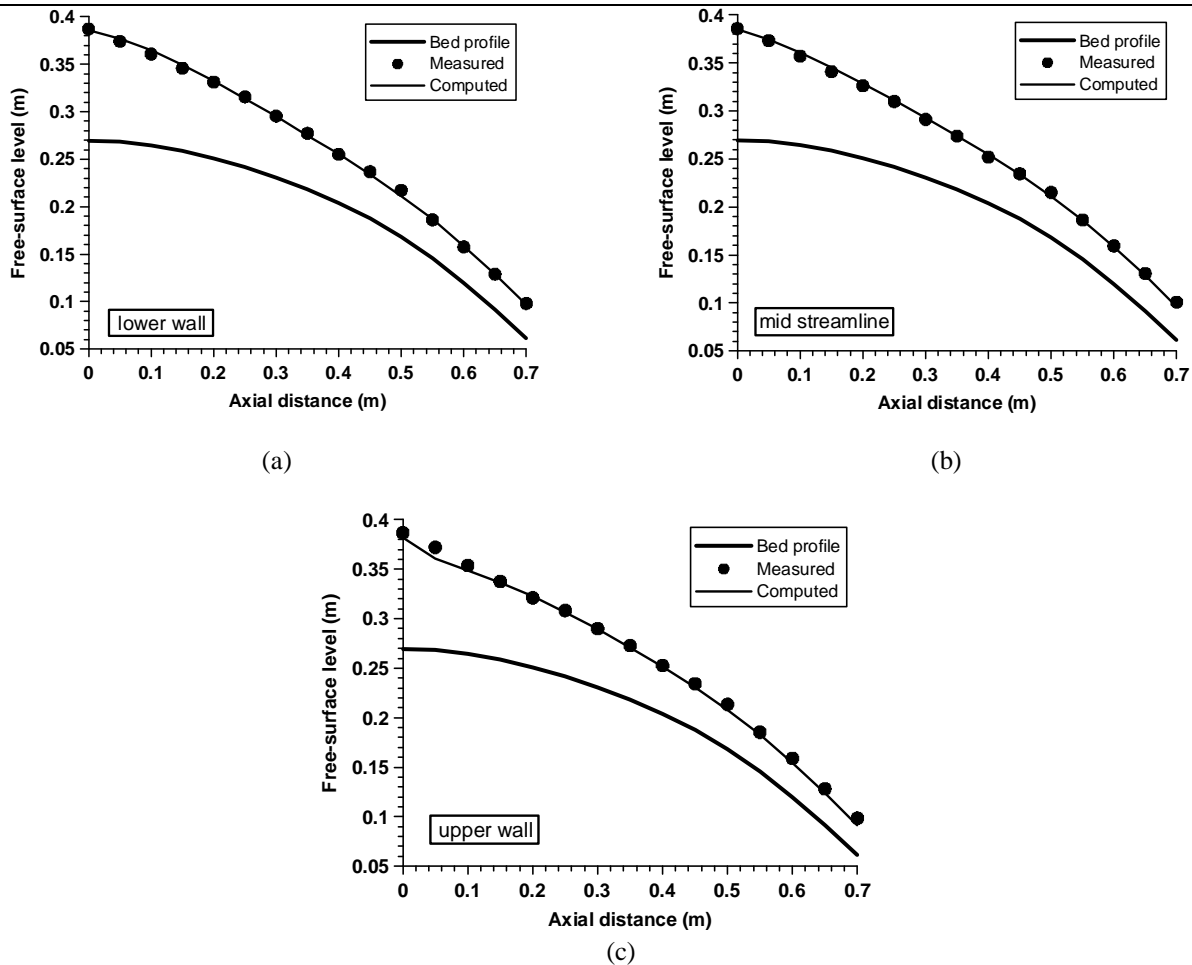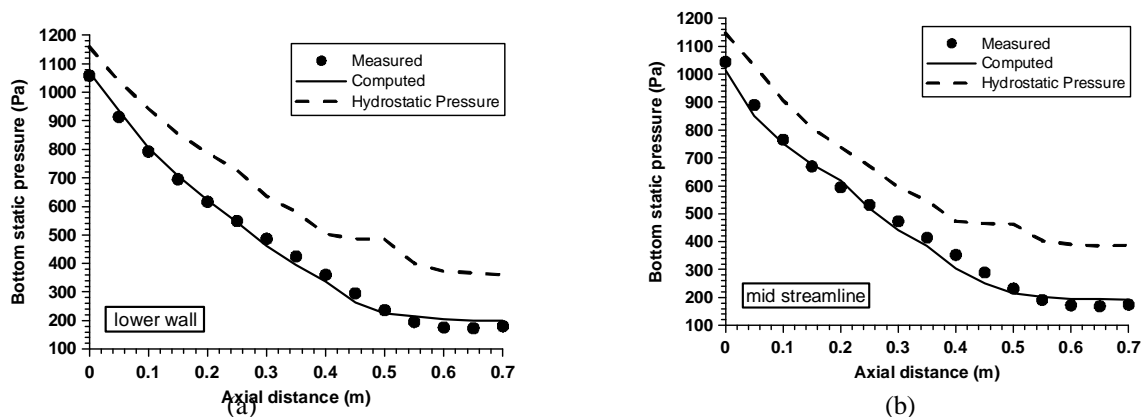
(a)

(b)

(c)

Figure 3. Comparison between measured and computed free-surface elevation (m) along: (a) the lower wall of the downstream spillway arc, (b) the mid-stream line of the downstream spillway arc and (c) the upper wall of the downstream spillway arc at Q=0.0163 m^3 s^{-1}

In figures 4a-4c calculated bottom static pressures are compared with the measured data along the, a) lower wall, b) mid-stream line and c) upper wall, respectively. Computed results satisfactorily agree with measurements.

(a)

(b)

Results from the above figures reveal a gradual pressure drop within the first 0.5 m measured downstream to crest. From this position towards to the end of the arc, the pressure drop decelerates. It is also evident that both measured and predicted bottom static pressures significantly diverge from the hydrostatic ones.
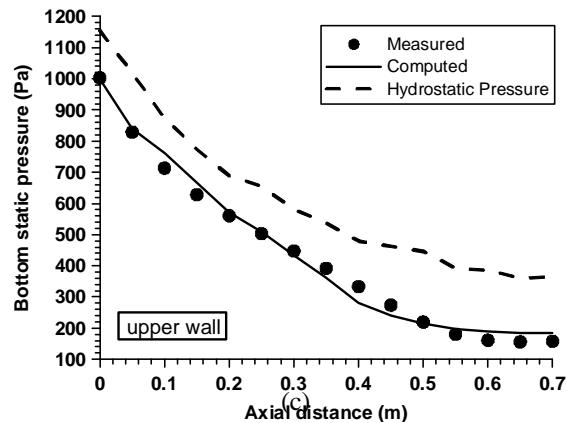

Figure 4. Comparison between measured and computed bottom static pressures (Pa) along: (a) the lower wall of the downstream spillway arc, (b) the mid-stream line of the downstream spillway arc and (c) the upper wall of the downstream spillway arc Q=0.0163 m^3 s^{-1}

Finally, it becomes apparent that away from the crest the flow is accelerated. Henceforth, the differences between computed and hydrostatic pressures increase.

3.2. Steady Flow over a Symmetric Weir

Sivakumaran et al [8] performed a series of experiments for steady flows over symmetric and asymmetric bedforms. All experiments were carried out in a 9.15 m long, 0.65 m high and 0.3 m wide horizontal flume made of a steel frame with glass side walls. The 1.5 cm thick plywood bed was elevated 0.1 m above the base of the flume, to host plastic tubes connecting the piezometer tapings placed along the centerline of the curved-bed model, with piezometers. The symmetric profile of the 1.20 m long weir is described with respect to normal distribution by the relation,

$$y = 20 \exp[-\frac{1}{2}(\frac{1}{24}x^2)] \tag{15}$$

x, y are the horizontal and vertical coordinates, respectively. The leading edge of the weir was placed 3.66 m downstream the flume's inlet. The leading edge water depth was measured as 0.3356 m and was used as an upstream boundary condition for the model. In the present work experimental data for a symmetric bedform are tested against current model predictions for a steady unit flow rate q=0.036 m3 s^{-1} m^{-1}. A structured grid consisting of hexahedra with a total of 41580 nodes was created. The flow was subcritical upstream the weir turning rapidly to supercritical at immediately downstream the crest. Therefore, boundary conditions with respect to transcritical flow were applied. A value of 1.0 was given to the pseudo-compressibility factor *β* while the Manning's roughness coefficient *n* was set 0.01 s m$^{-1/3}$ which is consistent with glass made walls and plywood bed. Figures 5a and 5b depict a comparison between measured and computed centreline water surface elevation and bottom pressure respectively.
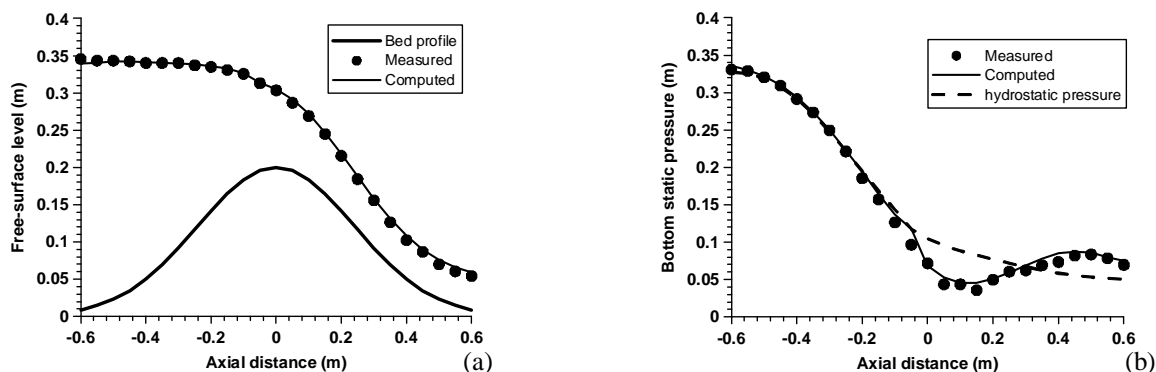

Figure 5. Comparison between measured and computed (a) water surface elevation (m) and (b) bottom static pressure (m) along the centreline of the symmetric weir after Sivakumaran et al, q=0.036 m^3 s^{-1} m^{-1}

Both comparisons show a very good agreement between measured and computed results. Also, figure 5b shows that the bottom pressure drops below the hydrostatic within a distance of 0.24 m downstream the crest.

3.3. Steady Flow over a Triangular Sharp Crested Sill

This section demonstrates the model's capability to capture water surface profiles during steady flow over a triangular shaped bottom sill with sharp crest. The experimental investigation was conducted by Farsirotou et al. [9] in a smooth, horizontal prismatic channel with rectangular cross-section of 6.0 m long, 0.076 m wide and 0.25 m high. The channel walls were made of 10.0 mm thick plexiglass. A triangular shaped sill of 0.38 m base length was placed on the bottom of the flume, at a distance of 1.90 m from the channel inlet, in a region of fully developed incoming flow. The construction was made of waterproof wood. The maximum sill height was equal to 0.051 m at an axial distance of 0.087m from its leading edge. Water surface profile measurements over the bottom sill, under equilibrium flow conditions, were obtained along the centerline of the model at different flow discharges. In the present test case three flow discharges were used; Q_1=0.93 l s^{-1}, Q_2=0.71 l s^{-1}, and Q_3=0.51 l s^{-1}. A relatively coarse grid consisting of 11700 nodes was adequate to simulate the developed flow accurately. Since the flow was subcritical upstream the sill turning rapidly to supercritical at immediately downstream the crest, boundary conditions with respect to transcritical flow type were applied. The pseudo-compressibility factor β was set equal to 1.0 while the value of 0.01 s m$^{-1/3}$ was given to Manning's roughness coefficient. In figure 6 measured water surface profiles are compared with the current model predicted ones, for the three aforementioned flow discharges respectively. The comparisons show a remarkable agreement between measurements and computed results.
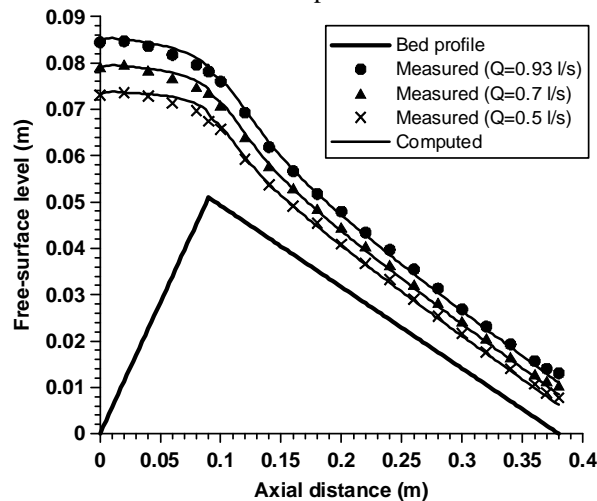

Figure 6. Comparison between measured, Farsirotou et al)and computed water surface profiles over the triangular shaped bottom sill, for Q=0.93 l/s, 0.7 l/s and 0.5 l/s

4. Conclusion

In the present study the development of a non-hydrostatic, 3D, implicit, finite-volume scheme, capable of simulating rapidly varied flows over irregular bedforms featuring weirs and spillways has been presented. By utilizing the pseudo-compressibility technique the modified Navier-Stokes equations were transformed in a non-orthogonal, body fitted local coordinate system and solved using a second order implicit scheme resulted from the linearization of the governing equations. Furthermore, the use of the two-dimensional depth-averaged mass continuity equation as a simplified aspect of determining the free-surface location was proved to be adequate enough for the simulation of various problems where rapid changes in the free-surface occur. To deal with significant numerical instabilities resulting from dispersion errors appearing during the fast grid reconstruction along the vertical direction, the use of a dual iteration step as a new idea was presented analytically. All calculations take place within the inner step while the outer step updates the calculated variables preparing thus for the next inner iteration step. The value of turbulent kinematic viscosity was determined empirically with respect to bottom friction velocity, assuming a linear distribution of bottom shear stress over the depth. The model was used to analyse steady flows over curved and sharp crested weirs. Predicted water surface elevations and bottom pressures were compared with measurements. Emphasis was given in the ability of the model to accurately simulate problems where non-hydrostatic pressure distribution occurs.

REFERENCES

[1] Bhajantri, M. R. and Eldho, T .I., 2007, Modeling hydrodynamic flow over spillway using weakly compressible flow equations. Journal of Hydraulic Research, 45(6), 844-852.

[2] Ferrari, A., 2010, SPH simulation of free surface flow over a sharp-crested weir. Advances in Water Resources, 33(3), 270-276.

[3] Haun, S., Reidar, N., Olsen, B. and Feurich, R., 2011, Numerical modelling of flow over trapezoidal broad-crested weir. Engineering Applications of Computational Fluid Mechanics, 5(3), 397–405.

[4] Chorin, A. J., 1967, A Numerical method for solving incompressible viscous flow problems. Journal of Computational Physics, 2(12).

[5] Liu, Z., 2001, Sediment transport. Laboratoriet for Hydraulik og Havnebygning Instituttet for Vand, Jord og Miljoteknik Aalborg Universitet, Finland.

[6] Klonidis, A. J., 2012, Computations and measurements of steady, three-dimensional flow with sediment transport around hydraulic structures. Ph.D. Thesis, Democritus University of Thrace, Department of Civil Engineering, Xanthi, Greece.

[7] Klonidis, A. J. and Soulis, J. V., 2001, An implicit scheme for steady two- dimensional free-surface flow calculation. Journal of Hydraulic Research, 39(3), 1-10.

[8] Sivakumaran, N. S., Tingsanchali, T. and Hosking, R. J., 1983. Steady shallow flow over curved beds. Journal of fluid mechanics, 128, 469-487.

[9] Farsirotou, E., Kotsopoulos, S., Xafoulis, N. and Sanatsios, G., 2014., Experimental investigation of non-uniform flow in rivers., Proc. 12th International Conference on Protection and Restoration of the Environment, Skiathos island, Greece, 873-880.